Surface rheological measurements of isolated food foam systems

Clarke, Christopher; Spyropoulos, Fotios ; Norton, Ian

DOI:
10.1063/1.5123664

License:
Other (please specify with Rights Statement)

Document Version
Peer reviewed version

Citation for published version (Harvard):
Clarke, C, Spyropoulos, F & Norton, I 2019, 'Surface rheological measurements of isolated food foam systems', *Physics of Fluids*, vol. 31, no. 9, 092002, pp. 092002-1-092002-11. https://doi.org/10.1063/1.5123664

Surface Rheological Measurements of Isolated Food Foam Systems

Christopher Clarke, Fotis Spyropoulos and Ian T. Norton*

*Department of Chemical Engineering, University of Birmingham, Edgbaston, Birmingham, B15 2TT, UK

Liquid foams represent a key component to a vast range of food industry products, from ice creams to the crema on coffee. Longevity of these foams is a highly desireable attribute, however in order for foam stability to be effectively controlled, a better understanding of the interdependence of the bulk liquid and air-liquid interfacial rheologies is required. This study follows an increasing trend in experimental investigations made of isolated foam structures at the microscale, where the bulk and surface dynamics of a single foam liquid channel can be accurately assessed. Isolated foam channels with adjoining nodes were studied for aqueous solutions of four food grade surfactants. Existing observations of distortions to Sodium Dodecyl Sulphate (SDS) channel geometries were confirmed for solutions of Tween 20 (T20) and Tween 80 (T80), and were well described by the theory presented here. Moreover, previously unseen distortions to liquid channels were observed for polymeric surfactant systems (hydroxypropyl methylcellulose (HPMC) and hydrolysed pea protein blend (HPP)), which were proposed to result from their high surface viscosities. The apparent surface viscosities, μ_s, of surfactants tested here ranged from high (10 g/s$< \mu_s <$10^{-3} g/s) for polymeric surfactants, to very low (10^{-10} g/s$< \mu_s <$10^{-8} g/s) for Tweens, clearly demarking the regimes of viscous and inertial dominant flows respectively. It is recommended that further work seeks to investigate the finding of a strong correlation between μ_s and channel surface tension, γ, for soluble surfactant systems, which could explain the apparent non-Newtonian values of μ_s that were consistently measured here.

1. Introduction

1.1 Background

The phenomenon of foam drainage is a complex multi-scale process that ultimately leads to the collapse of foams due to film rupture and bubble coalescence[1]. Foam longevity is a common problem in the food industry, where the instability of liquid foam products such as whipped toppings, ice cream, mousses and confectionary fillings can dramatically decrease their potential shelf life[2].

As a key mechanism underlying foam collapse, arresting liquid drainage through the network of channels or Plateau borders (PBs) between bubbles is often a key focus in foam formulation. In many food products (and indeed non-food products) this is still largely addressed by increasing the bulk liquid viscosity using a trial and error approach[3]. The ultimate goal in these instances is to create a yield stress of the bulk liquid that cannot be reached by the action of gravitational forces alone, therefore halting liquid flow altogether.

More recently, the drive to improve our understanding on food ingredients has led to an increasing number of innovations in formulation and processing that target drainage via other means. Examples range from the blocking of liquid channels using novel particle systems[4], to creating more robust interfacial structures that increase the channels' hydrodynamic resistance with varying combinations of surface active particles, low molecular weight surfactants (LMWS) and polymeric surfactant systems[2,3].

As the development of novel food microstructures and foam formulations continues, the need to better understand the role played by the air-liquid interface in foam drainage is becoming increasingly apparent. Different surfactants dramatically alter the physical properties of the interface, whose surface rheology and subsequent impact on liquid flow are still extensively studied in both liquid films and foam channels alike.[5-12]

Theoretical modelling of foam channels has presented a significant challenge to researchers[13]. The already complex geometries within the foam microstructure undergo expansion and distortion, with these phenomena determined, to an extent, by the rheology of the bulk liquid and the gas-liquid interface, which themselves are dependent on the liquid flow rate[14]. In addition, the body of experimental work studying these isolated channels is extremely limited[15], making it difficult to clearly confirm or refute theoretical predictions. When one considers that many studies of macroscopic foam systems are based on such microscale theory, it is clear that more microscale evidence is required[16], in terms of both quantity and accuracy.

The most recent experimental studies of isolated PB and PB-Node geometries have proved to be a step forward with respect to understanding channel surface rheology. By creating spatially 'ideal' arrangements of foam channels within bespoke frames, researchers have been able to probe specific physical and chemical variables thought to influence the nature of the interface[15,6,7,17-21]. Such in-situ measurements of channel surface rheology are critical, as they provide unparalleled control and measurement consistency.

So far, the study of these isolated systems has been limited to simple LMWS systems such as Tetradecyltrimethylammonium Bromide (TTAB)[19-21] and Sodium Dodecyl Sulphate (SDS)[6,19,20] with variations in interfacial rheology introduced by small additions of dodecanol (DOH), and bulk rheology by the addition of glycerol. Most recently, the work by Clarke *et al.*[6] using an isolated PB-Node system with pure SDS solution, has yielded surprising findings regarding previously unobserved changes to fundamental liquid channel geometries during forced liquid flow. In addition, these results appear to confirm what are purported as the most accurate surface viscosity measurements of SDS to date[22], predicting the air-liquid interface of SDS and other soluble LMWS systems to be so low as to be considered virtually inviscid.

The surface shear viscosity, relates the shear force per unit length of interface to an applied shear rate[23], which in PB systems arises from liquid flow adjacent to the interface. Higher values of surface viscosity result in greater dissipation of liquid flow at the PB boundaries, resulting in increasingly Poiseuille-like flow velocity profiles[24]. The contrast between low and high surface viscosity is thought to be responsible for the two macroscopic regimes of *node-dominated* and *channel-dominated* foam drainage respectively, which describe whether the bulk of flow dissipation is thought to occur at the nodes or within the PBs themselves [6,19,25]. The extremely low values of surface viscosity found by Zell *et al.*[22] and Clarke *et al.*[6] for

soluble LMWS systems therefore suggests that flow dissipation occurs primarily in the nodes in these cases, with surface viscosity having little impact on macroscopic foam drainage.

As the theory used by Clarke *et al.*[6] was unable to describe the full extent of the unusual PB geometries identified, and based only on results from SDS solutions, the present study aims to further probe this promising measurement technique. In order to do this, the current work assesses a range of surfactant solutions that are anticipated to display a wide range of surface viscosities. In order to maximise the relevance of these results to the food industry, formulations investigated here reflect the diversity of food grade surfactants ranging from soluble LMWS systems (similar to SDS) to polymeric surfactant systems such as proteins and long chain polysaccharides. The theory used by Clarke *et al.*[6] has been assessed and potentially revised if it is to account for the unusual PB geometries that were previously observed for SDS.

1.2 Theory

1.2.1 The PB Relaxation Equation

In the previous study by Clarke*, et al.*[6], a simplified solution to the standard drainage theory (Eq. 1)[16] was fitted to vertical geometric PB profiles measured for 0.5wt% SDS solution at a range of liquid flow rates, Q, and PB lengths, l_1. This solution is shown in Eq. 2, the derivation of which is laid out by Elias*, et al.*[7] and describes the relaxation of the PB radius between the limits of an initial radius, R_0, at the vertical height $Z = 0$, and an equilibrium radius, R_e, over a vertical distance set by the relaxation length, L.

$$\frac{dR}{dZ} = \frac{cD\nu Q - gc^2R^4}{\left(\frac{2IQ^2}{R}\right) - \left(\frac{c^2R^2\gamma}{\rho}\right)} \tag{1}$$

$$R = R_e + (R_0 - R_e)e^{-Z/L} \tag{2}$$

The equilibrium radius is defined by Eq. 3, describing the lower limit of the PB radius, at which gravitational and capillary forces are balanced. Here c is a geometric constant (~ 0.161), ν is the kinematic viscosity of the solution, g is the acceleration due to gravity and D is the viscous flow parameter:

$$R_e = \left(\frac{D\nu Q}{cg}\right)^{1/4} \tag{3}$$

The relaxation length, L, is described by Eq. 4 and includes the effects of surface tension, γ, solution density, ρ, and inertial contributions to liquid flow via the inertial flow parameter, I.

$$L = \frac{IQ^2}{2c^2g{R_e}^4} - \frac{\gamma}{4\rho g R_e} \tag{4}$$

As a simplified solution to Eq. 1, Eq. 2 was easily applied to measured PB geometric profiles using automated fitting methods. The obtained values of the fitting parameters R_e and L were then used to calculate the physical variables D and I from Eq. 2 and 3 respectively, using pre-measured values of ν, ρ, Q and γ. Here it was assumed that the surface tension, γ, was equal to its equilibrium value as measured by Wilhelmy Plate measurements ($\gamma = \gamma_{eq}$) and also independent of liquid flow rate and PB length.

The parameters D and I ultimately describe the shapes of the PB velocity profiles according to Eq. 5 and 6, where individual flow velocity components, u, across a given PB cross section give the average flow velocity, $\bar{u} = U$.[7]

$$D = -R^2\overline{\Delta u}/\bar{u} \tag{5}$$

$$I = \overline{u^2}/\bar{u}^2 \tag{6}$$

Flow velocity profiles lie between the two extremes of Poiseuille flow and Plug flow, which are described by $D \to 312$, $I > 1$, and $D \to 0$, $I \to 1$, respectively[7]. Low molecular weight surfactants such as SDS and Polysorbates/Tweens are generally expected to fall into the latter category, as their extremely high mobility at the air/water interface[22] results in minimal viscous dissipation of liquid flow at the PB boundaries.

The values for the viscous flow parameter, D, were converted into values for the dimensionless Boussinesq Number, B_0, and its dimensional counterpart, the surface shear viscosity, μ_s, using the phenomenological expression proposed by Nguyen[26] (Eq. 7) and the definition of the surface shear viscosity given by Eq. 8. It should be noted that Eq. 7 is only valid for a straight, vertical PB, and therefore these calculations were applied only to the equilibrium case $R = R_e$.

$$D^{-1} = c\left[0.02 + \frac{0.0655{B_0}^{-0.5}}{0.209+{B_0}^{0.628}}\right] \tag{7}$$

$$\mu_s = B_0\mu R \qquad (\text{with } R = R_e) \tag{8}$$

Despite Eq. 2 being a good description of PB geometric profiles exhibiting relaxation, Clarke *et al.*[6] found that increasing proportions of the profile were replaced with expansion into the adjoining node at decreasing liquid flow rates and PB lengths (see Fig. 1). As such, these expansion regions were excluded, resulting in an incomplete analysis of the PB profiles. Furthermore, the unusual nature of the transitions between relaxation and expansion at $Z = Z_{swell}$ and their PB length and flow rate dependence requires explanation, as a potential change in the physical parameters of the system might be suggested.

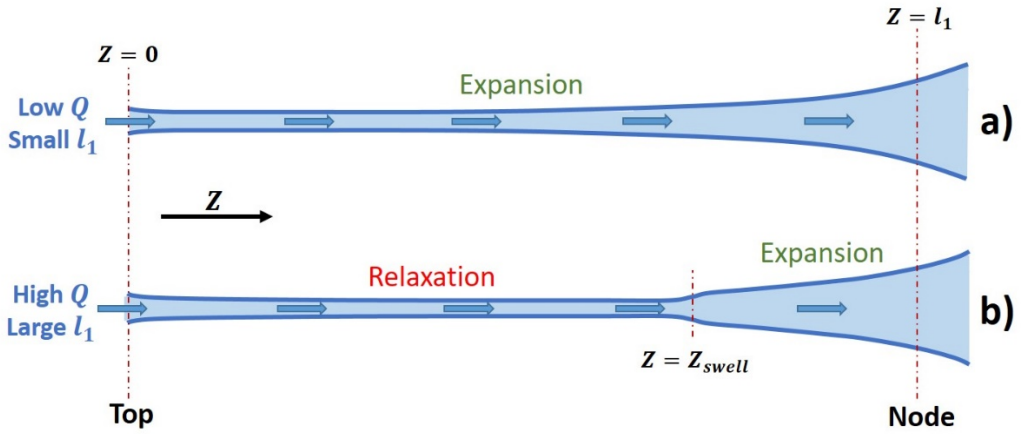

Figure 1. Visualisation of PB profiles of length, l_1, and liquid flow rate, Q. a) Low Q, small l_1 resulted in almost complete expansion profiles. b) Increasing Q and l_1 exhibited both relaxation and expansion with increasingly prominent transition distortions at height $Z = Z_{swell}$ [6].

1.2.2 The Relaxation-Expansion PB Profile Equation

In order to address the inability of Eq. 2 to describe PB expansion, a full geometric profile solution was derived from Eq. 1. The variables: D, ν, Q, g, c, I, γ and ρ in Eq. 1 were once again substituted for R_e and L using Eq. 3 and 4, with an additional term, the capillary length, $L_c = \sqrt{\gamma/\rho\, g}$. Eq. 9 sets up the solution to this revised form of Eq. 1 as an integral with the limits of the initial radius, R_0, at $Z = 0$ to some radius R at a distance Z from $Z = 0$. Eq. 9 was solved using the computer algebra system, Maxima (VA Software, USA), yielding Eq. 10; a complete geometric PB profile solution.

$$\int_0^Z dZ = \int_{R_0}^{R} \left\{ \frac{{L_c}^2}{R(R_e+R)} + \frac{{L_c}^2 R_e}{({R_e}^2+R^2)(R_e+R)} + \frac{4L{R_e}^4}{R({R_e}^4-R^4)} \right\} \cdot dR \tag{9}$$

$$Z = L\, ln\left[\frac{R^4({R_0}^4-{R_e}^4)}{{R_0}^4(R^4-{R_e}^4)}\right] + \frac{{L_c}^2}{4R_e}\left\{ ln\left[\frac{R^4(R_0+R_e)^2({R_0}^2+{R_e}^2)}{{R_0}^4(R+R_e)^2(R^2+{R_e}^2)}\right] + 2\, tan^{-1}\left[\frac{R-R_0}{R_e(1+RR_0/{R_e}^2)}\right]\right\} \tag{10}$$

Eq. 10 gives two sets of solutions of a single set of physical variables, one describing PB relaxation (closely approximated by Eq. 2) and the other PB expansion (see Fig. 2). These solutions join at a minimum occurring at $Z = 0$, $R = R_0$; resulting in the initial condition given by Eq. 11:

$$R_0 = \left(\frac{2\rho I Q^2}{c^2\gamma}\right)^{1/3} \tag{11}$$

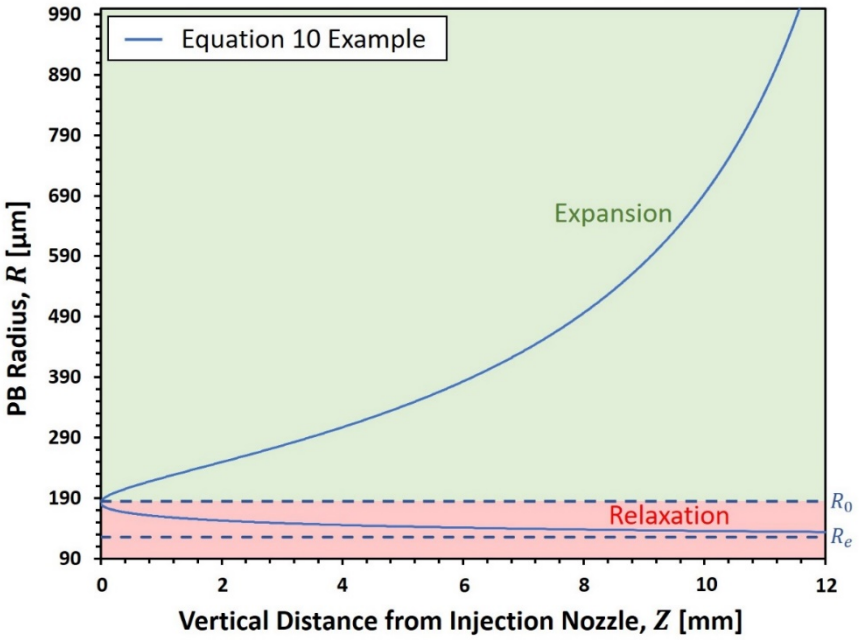

Figure 2. Eq. 10 example, demonstrating simultaneous relaxation and expansion solutions. Solutions meet in the minimum occurring at $R = R_0, Z = 0$, while the relaxation solution tends to $R = R_e$ as $Z \to \infty$.

The initial condition set by Eq. 11 is striking, as it shows a dependence of R_0 on bulk and surface liquid properties, as well as liquid flow rate. When one considers the case of PB expansion into an adjoining node, both the rate of expansion (dR/dZ) and the initial radius

from which this expansion can commence are shown to be dependent on the bulk and surface parameters of the liquid (Eq. 1 and 11). Furthermore, the final radius of this expansion must coincide with the initial radius of the adjoining node, R_{no}, at a height $Z = l_1$ (see Fig. 1). In a forced flow system where the value of l_1 is primarily set by the length of the frame geometry producing the PB-node system, there are limited ways in which the above conditions can be satisfied. The first would require a significant change in the physical parameters I, D and γ as the PB transitions from the relaxation to the expansion state. The second would require an offset of the zero height of the expansion solution, Z_T, allowing I, D and γ to remain the same as for the relaxation solution, but providing a smooth transition into the node at R_{no} (see Fig. 3). The third would require a combination of both these effects, wherein changes to I, D and γ are minimised by the zero offset of the expansion solution.

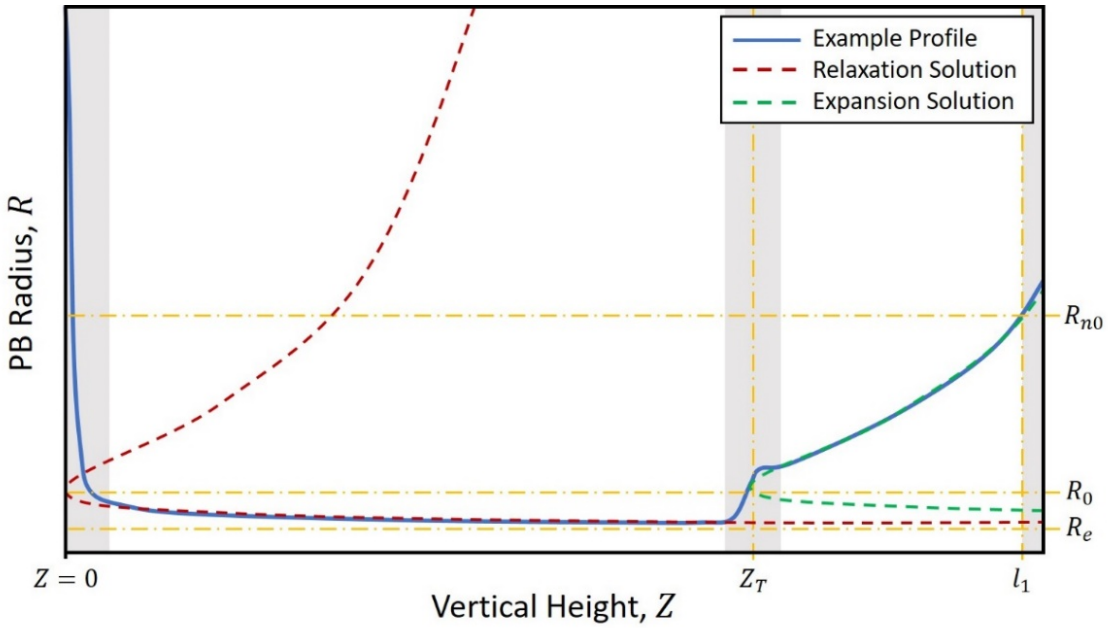

Figure 3. Relaxation (red) and expansion (green) solutions against an example PB profile (blue), with key coordinates marked (yellow). Zero or small variations in the physical parameters I, D and γ between relaxation and expansion solutions require a zero offset Z_T. Grey regions represent parts of the profile unaccounted for in the current theory, namely: The distortion of caused by the PB attachment to the frame, the transition from relaxation to expansion solutions, and the node.

A revised form of Eq. 10 is given by Eq. 12 wherein the zero offset, Z_T, is incorporated. It is important to note that this amendment is only necessary in the context of a fixed point of reference for $Z = 0$.

$$Z - Z_T = L\,ln\left[\frac{R^4\left({R_0}^4-{R_e}^4\right)}{{R_0}^4\left(R^4-{R_e}^4\right)}\right] + \frac{{L_c}^2}{4R_e}\left\{ln\left[\frac{R^4(R_0+R_e)^2\left({R_0}^2+{R_e}^2\right)}{{R_0}^4(R+R_e)^2\left(R^2+{R_e}^2\right)}\right] + 2\,tan^{-1}\left[\frac{R-R_0}{R_e\left(1+RR_0/{R_e}^2\right)}\right]\right\} \quad (12)$$

2. Experimental

2.1 Preparation of Solutions

Tween® 20 and Tween® 80 from Sigma-Aldrich (UK), Methocel™ F50 from The Dow Chemical Company (USA), and Hyfoama™ (pea) from Kerry (Ireland) were selected for

investigation, due to their ability to quickly form stable films while representing stabilisation mechanisms dependent upon surface viscosities at opposite ends of the spectrum.

Tween 20 and Tween 80 represent two commonly used soluble surfactants in the food industry, where Tween 20 in particular is regularly used in foaming applications. The Gibbs-Marangoni stabilisation mechanism of these LMWS systems is reliant upon the high mobility of surfactant molecules at the interface, therefore yielding extremely low surface viscosities[22].

In contrast, the stabilisation mechanism of most polymeric surfactants is to form a more robust network through the cohesive interaction of adsorbed polymers at the interface, resulting in significantly higher values of surface viscosity[3]. Methocel™ F50 consists of the long chain polysaccharide Hydroxypropyl methylcellulose (HPMC), with controlled degrees of methoxyl and hydroxypropyl substitution improving its film forming ability. It is claimed to exhibit surface gelation at the air-liquid interface, with higher bulk concentrations leading to increased gel strength[27]. As such, this represents a potentially extreme case of a virtually immobile air-liquid interface, which would therefore be expected to yield very high values of surface shear viscosities. The surface active component of the Hyfoama™ used in this study were pea protein hydrolysates (HPP), these having been found to exhibit far greater functionality than their native pea protein isolates[28]. Hyfoama™ has not been reported to exhibit surface gelation, and was therefore expected to yield lower values of surface shear viscosity than for Methocel™ F50.

Surfactants were weighed using a digital balance to an accuracy of three decimal places. Purified water (15.0 MΩ·cm) was weighed into borosilicate glass beakers and magnetically stirred at room temperature while surfactants were added. Stirring continued for a minimum of 30 minutes after all surfactant was visibly in solution in order to ensure full incorporation of surfactant and solution homogeneity. A minimum of 60 minutes stirring was used for HPMC preparation, as this was required to ensure its complete hydration.

2.2 Characterisation of Surfactant Solutions

Two solution concentrations of each surfactant were chosen for analysis, details of which can be found in Table 1. In the case of polymeric surfactants, initial concentrations were chosen based on the solutions' ability to reliably form stable films within the PB-Node Setup. These concentrations were subsequently doubled and trialled again for comparison. Concentrations of Tween 20 and Tween 80 were selected to be ∼10× and ∼20× the literature CMC values[29,30], as these would serve to test the assumption that constant equilibrium surface tension values can be assumed in PBs for surfactants well above their CMC concentrations (i.e. $\gamma \equiv \gamma_{eq}$). To the knowledge of these authors, there is no instance of this assumption ever having been tested, most likely due to the difficulties in doing so. It is highly possible however; that the variations in channel geometries and shears associated with different liquid flow rates could affect these values.

Bulk properties ρ and μ were measured in triplicate using a Krüss Processor® Tensiometer K100 (Krüss GmbH, Germany) with density hook attachment and silicon density standard, and a Malvern Kinexus® Pro rheometer (Malvern Panalytical, UK) with Double-Gap geometry respectively. Reference values for the solution surface tensions, γ, were measured in triplicate

using a Krüss Processor® Tensiometer K100 (Krüss GmbH, Germany) with Wilhelmy Plate attachment. All property values were averaged with absolute errors of one standard deviation.

2.3 The PB-Node Setup

The isolated PB-Node setup used to create and observe the desired PB-Node geometries is well described by Clarke, *et al.*[6]. This forced flow setup consisted of a closed 3-legged frame that could be submerged and withdrawn from surfactant solution to produce an ideal PB and node configuration (Fig. 4). The selected frame geometry produced PB lengths of $l_1 \approx 25.5$ mm, as this maximised the amount of experimental data to fit to while still producing stable PB-Node systems. Backlit profiles of the PB-Node geometries were imaged and processed to allow fitting of Eq. 12.

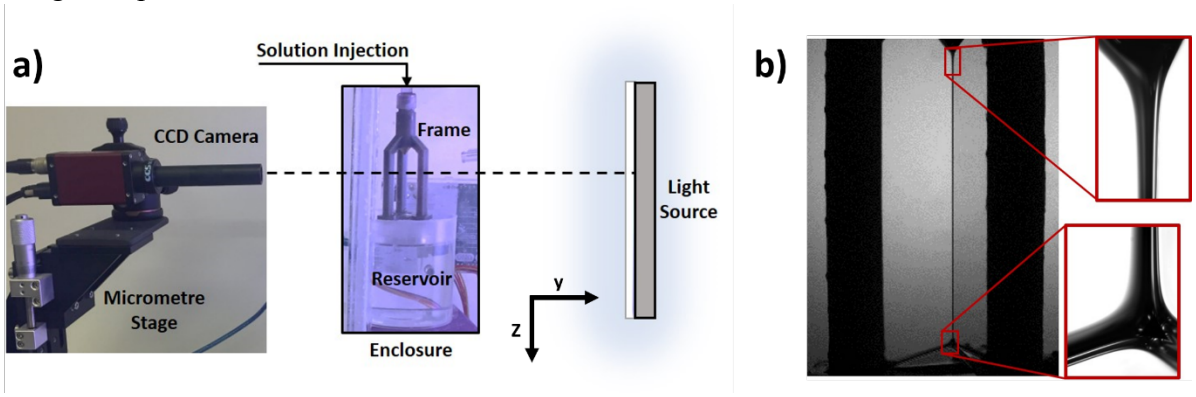

Figure 4. Imaging for analysis of PB-Node profiles. a) Optical Setup - A camera images the enclosed frame using a rear diffuse panel light to create shadow profile images. b) Low and high magnification images of a PB node profile, where highest magnification (red highlighted images) represents 1.5 µm per image pixel.

Controlled liquid flow rates, Q, were achieved by injecting surfactant solution directly into the upper PB at increments of 20 µl/min in the range 20 µl/min $\leq Q \leq$ 180 µl/min, therefore describing conventional drainage flow rates (0 µl/min $\leq Q \leq$ 100 µl/min) and beyond. By using this broad range of liquid flow rates, any flow rate dependent trends of fitting variables were expected to become more apparent. Once equilibrium was achieved at each flow rate, PB profile widths were acquired from images taken at increments along the full PB length, using an image processing technique developed by Clarke, *et al.*[6]. Image resolutions varied between 1.5µm/Pixel to 10µm/Pixel depending upon the necessary magnification for given PB widths. These were used to calculate PB radii, R, for the full PB profiles, starting from $Z = 0$ at the injection nozzle to $Z \approx l_1$.

2.4 Model Fitting

The fitting parameters, R_e, I, γ and Z_T were used to fit Eq. 12 to measured PB profiles, where Q was controlled and ν, ρ were directly measured from the liquid solutions (see below). While Clarke *et al.*[6] had previously assumed that constant γ, where $\gamma = \gamma_{eq}$, could be applied for SDS solutions, these resulted in some values of I below their physical limit of 1 when fitting Eq. 2. In this study, I was restricted to its physical lower limit of 1. As a result, the only means by which quality fits could be achieved was by allowing for variations in γ.

Utilising automated fitting methods in this study represented a significant technical challenge. This was due in part to the complexity of Eq. 12, but also to a number of poorly characterised distortions and transitions in the PB profiles (see Fig. 3). Ultimately, it was shown that manual fitting was consistently able to produce better quality fits to experimental data than automated methods at this stage.

The initial attempts to fit Eq. 12 to PB profiles exhibiting simultaneous relaxation and expansion without the inclusion of a zero offset (i.e. $Z_T = 0$), were found to be completely unsuitable. In these instances, even vaguely appropriate fits required values for the surface tension to be higher than that of pure water, making them unfeasible as solutions. As such, it was assumed that in these cases $Z_T > 0$ for expansion solutions and that this would have served to minimise or remove variations in D, I and γ over the length of the PB at constant liquid flow rates. In order to assess whether this was the case, potential solutions were further limited such that the fitting variables R_e, I and γ were the same for both relaxation and expansion solutions at any given liquid flow rate.

2.5 Measurement of Relaxation-Expansion Transition Points

The distinctive transition regions between profile relaxation and expansion observed by Clarke, *et al.*[6] became increasingly evident with increasing values of l_1 and liquid flow rates, Q. These regions were estimated based on measured PB profiles, where the transition spanned the end of consistent PB relaxation behaviour to the beginning of consistent expansion behaviour (see Supplementary Material S1). No visible transition regions were recorded for PB profiles showing expansion only (i.e. $Z_T < 0$).

3. Results

3.1 Solution Properties

Values for specific bulk and surface properties of surfactant solutions are presented in Table 1, where measured density, ρ, and dynamic viscosity, μ, were used in subsequent calculations of the surface shear viscosity, μ_s, according to Eq. 2 and 7, where $\nu = \mu/\rho$. Dynamic viscosity of the Tween solutions showed the anticipated minor increase in Newtonian viscosity from pure water ($\mu \approx 8.9\times10^{-4}$ Pa·s at 25°C)[31] with increasing concentration. The viscosity of polymeric surfactants showed shear thinning behaviour, requiring the ability to determine appropriate viscosities for given liquid flow rates through their PBs. In order to do this, Eq. 13[7] was used to calculate the average shear rate, $\overline{\dot{\gamma}_s}$, of a PB cross section with radius, R. While this provides an excellent representation of shear rates adjacent to the PB interface for plug flow-like velocity profiles ($D \to 0, I \to 1$), it was duly noted that gradually Poiseuille-like flow profiles ($D \to 312,\ I > 1$) would increasingly overestimate shear rates adjacent to the interface. As such, it was anticipated that small underestimations of dynamic viscosity in shear thinning samples would be made, causing an artificial increase in the calculated values of D according to Eq. 3. This was taken into account in the subsequent analysis of HPMC and HPP results (see Supplementary Material S2).

$$\overline{\dot{\gamma}_s} \approx \frac{Q}{cR^3} \tag{13}$$

Surfactant & Concentration [wt%]	Density [mg/ml]	Viscosity [Pa·s] ($\times 10^4$)	Average Surface Tension [mN/m]
0.075wt% Tween 20	997.7 ± 0.3	9.56 ± 0.07	36.28 ± 0.22
0.150wt% Tween 20	997.9 ± 0.1	10.23 ± 0.48	34.76 ± 0.37
0.020wt% Tween 80	997.9 ± 0.1	8.84 ± 0.03	40.01 ± 0.51
0.039wt% Tween 80	997.6 ± 0.4	9.69 ± 0.23	39.24 ± 0.47
3.700wt% HPP	1011.0 ± 0.4	13.20 ± 0.20	43.24 ± 0.52
7.400wt% HPP	1025.8 ± 0.4	15.23 ± 0.65	41.59 ± 0.36
1.000wt% HPMC	1000.0 ± 0.1	90.20 ± 6.43	46.89 ± 0.41
2.000wt% HPMC	1002.6 ± 0.5	412.94 ± 1.43	48.09 ± 0.68

Table 1. Averaged results of triplicate measurements of physical properties of surfactant solutions with associated errors of one standard deviation.

3.2 Model Fitting

Measured profiles of Tween 20 and Tween 80 were found to be similar to those described by Clarke *et al.*[6], producing the anticipated flow rate dependent transitions from relaxation to expansion with increasing liquid flow rates (see Fig. 1). A typical profile example of this is shown in Fig. 5 for 0.075wt% Tween 20 at Q=140 µl/min, alongside the corresponding flow rate profile measured for 2wt% HPMC. Eq. 12 was consistently able to describe both relaxation and expansion profiles for both Tween systems with a single set of values for R_e, I and γ. R-squared values confirmed this with an overall range of 0.70≤ R-Squared<1.00, and an average of 0.96. The poorest fits consistently occurred at flow rates closest to the transition from $Z_T < 0$ (Fig. 1a) to $Z_T > 0$ (Fig. 1b), where separate relaxation and expansion regions began to appear. This was hypothesised to be the result of rapid fluctuations between these two profile states, which were observed during image acquisition and resulted in a superposition of these states in the final PB profiles.

The measured profiles of HPMC and HPP had substantially higher radii than those for the Tween systems, yielding a previously unseen profile geometry. Fig. 5 shows a typical example, where a solution of 2.0wt% HPMC quickly approached its equilibrium radius, R_e, before suddenly decreasing in radius as the PB transitioned into the node at $Z \approx l_1$. It is proposed that this node transition represents the case where R_e exceeds the initial node radius, R_{n0}, ($R_e > R_{n0}$) in contrast to the LMWS PB distortions that ultimately resulted from $R_e < R_{n0}$.

The lower magnification required to obtain images of the polymeric surfactant PBs increased the error margins in measured values of R_e. This made it difficult to assess whether or not any relaxation of the PB profile was due to measurement error, meaning that fitted values of γ and I could vary substantially without a marked effect of fit quality. As such, values of γ and I were neglected for further analysis for HPMC and HPP.

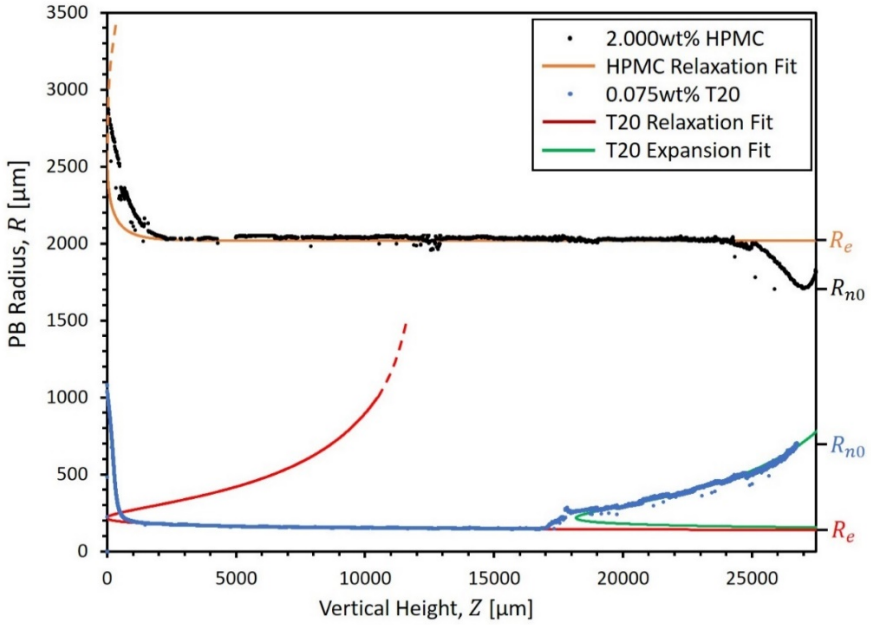

Figure 5. Measured profiles of 0.075wt% Tween 20 and 2wt% HPMC at Q=140µl/min, with corresponding fits of Eq. 12. Two distinctive profile distortions emerge based on whether $R_e > R_{n0}$ (HPMC) or $R_e < R_{n0}$ (Tween 20).

3.3 Relaxation-Expansion Transitions

The transitions between PB relaxation and expansion were well described by Eq. 12, as shown in Fig. 6. Values of $Z_T > 0$ matched well with visible transition regions between relaxation and expansion solutions, whereas $Z_T < 0$ resulted in the full profile being dominated by expansion into the node (Fig. 1a). Once again, profiles closest to the transition between $Z_T > 0$ and $Z_T < 0$ were shown to produce the poorest match between Z_T and visible transitions, owing to the suspected superposition of these two states in the measured PB profiles. Overall, it was shown that Eq. 12 was able to produce a very accurate description of the measured PB profiles, including the flow rate dependent variations in relaxation-expansion transitions.

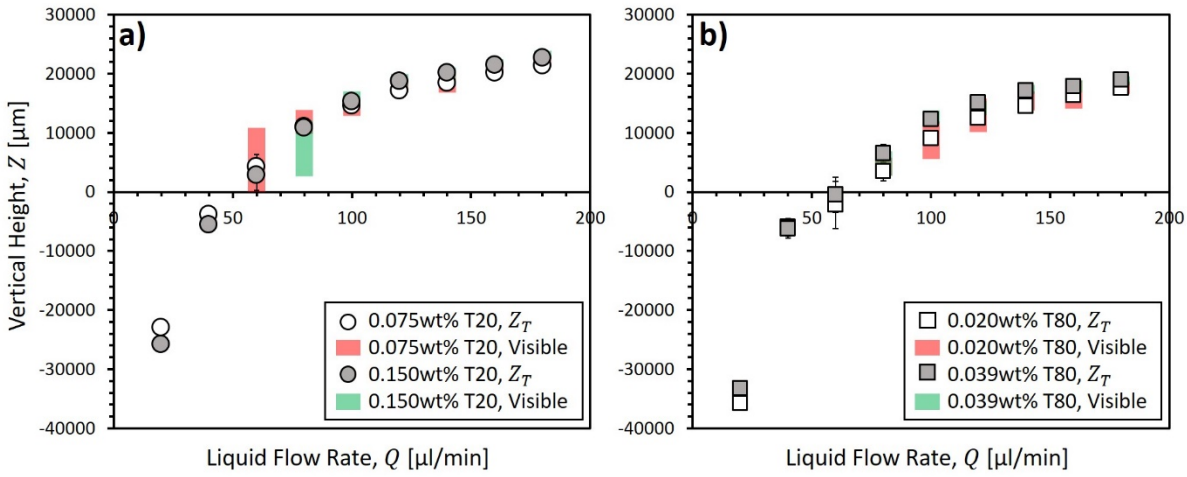

Figure 6. Comparison of the fitted profile offset, Z_T, for a) Tween 20 and b) Tween 80 solutions to their visible relaxation-expansion transitions first observed by Clarke, *et al.*[6]. The full range of Z covered by the visible transition regions are highlighted by red and green bars.

3.4 Fitting Parameters

The fitted surface tension, γ, for solutions of Tween 20 and Tween 80 at discrete liquid flow rates are shown in Fig. 7. Surface tension increased with liquid flow rate until the critical point at which relaxation and expansion solutions separated (i.e. $Z_T > 0$), after which it began to decline once more (Fig. 7a and 7b). Minimum values of γ approach the measured equilibrium surface tensions, γ_{eq}, of each solution. While an in-depth study of surface tension variability is beyond the scope of the current study, it was clearly observed that surface tension increased with calculated values of the apparent surface viscosity, μ_s (Fig. 7c and 7d). As surface tension varies inversely with the surfactant concentration at the air-liquid interface[32], this would suggest that less surfactant at the interface caused an increase in the apparent surface viscosity. This counterintuitive result is explained when one considers that the range of apparent surface viscosity values calculated here was in the range 10^{-10} g/s$< \mu_s <10^{-8}$ g/s, while the surface shear viscosity of pure water is approximately 1.2×10^{-5} g/s[33]. Therefore, it follows that a decreased population of surfactant species must increase the surface viscosity as a pure air-water interface is approached.

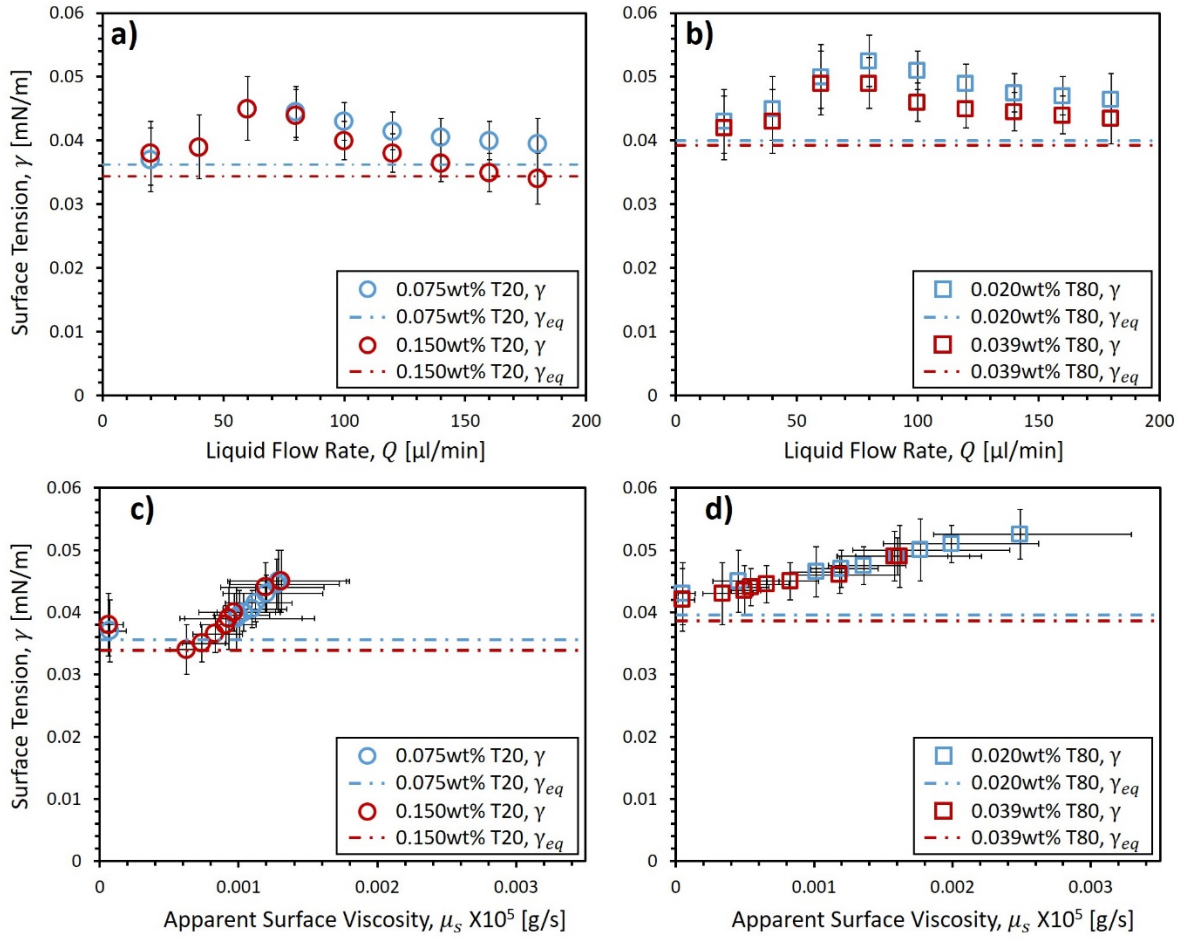

Figure 7. Surface Tensions, γ, from fits of Eq. 12 to a) & c)Tween 20 and b) & d) Tween 80 PB profiles. a) & b) show the relationship between γ and Liquid Flow Rate, Q, while c) & d) show the relationship between γ and the Apparent Surface Viscosity, μ_s, calculated from Eq. 3, 7 and 8.

Values for the inertial flow parameter, I, of Tween solutions can be found in Fig. 8, where they are plotted alongside the calculated values of the viscous flow parameter, D, for the equilibrium PBs ($R = R_e$). As discussed in Section 1.2.1 (Eq. 5 & 6), the values of I and D describe the flow velocity profiles, where $I \to 1$ as $D \to 0$ as perfect plug flow is approached. This relationship was well described by Fig. 8, and matches well with the finding of a virtually inviscid interface for the PBs calculated here. The size of the error margins in I made it difficult to draw any firm conclusions on the impact of the different surfactants on the I-D relationship, however combining all solutions indicated the same fundamental trend.

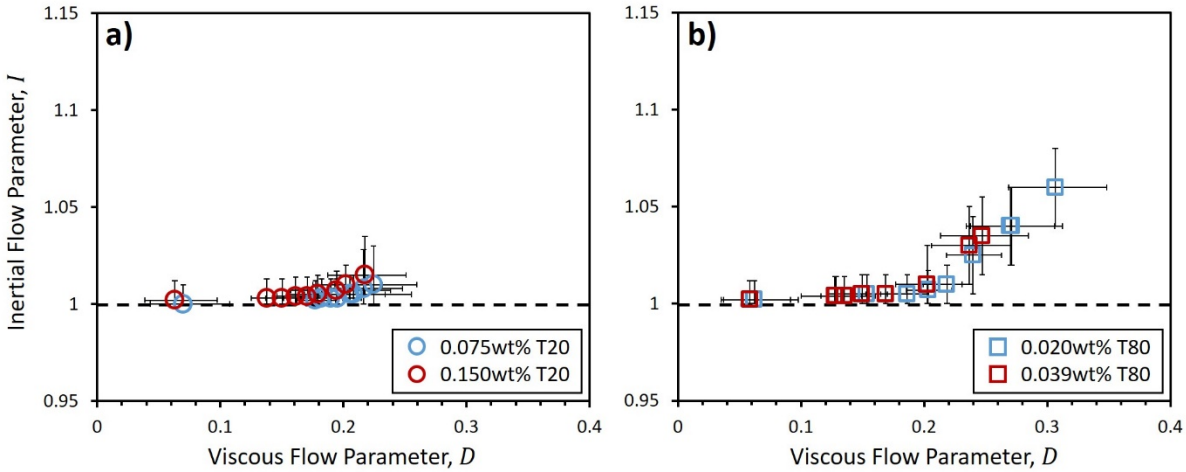

Figure 8. Inertial Flow Parameters, I, vs. Calculated Viscous Flow Parameters, D, from fits of Eq. 12 to a) Tween 20 and b) Tween 80 PB profiles. Black dashed line represents a value of 1 and the physical lower limit of I.

Despite it not being possible to establish meaningful values of I and γ for polymeric surfactant solutions, the calculated values of D from the fitted equilibrium radii, R_e (Eq. 3), could still be compared to LMWS solutions. Fig. 9 shows that values of D for solutions of HPMC and HPP lay at the opposite end of the spectrum from the Tween solutions, approaching the limits of an immobile interface as $D \to 312$. As a general trend, it was noted that the average D value (and consequently μ_s) for a given surfactant solution strongly related to its average liquid shear rate, with high D producing lower liquid shear rates and *vice versa*. Visualisations of the kind of flow velocity profiles expected between these low mobility and high mobility regimes are shown in the relevant regions of Fig. 9.

Values of μ_s for HPMC were calculated to range from 10^{-1}g/s< μ_s <10^{1}g/s for 2.0wt% and to be consistently of the order 10^{-2}g/s for 1.0wt% concentration. This was a strong indication that these concentrations produced the gelled PB interfaces described in Section 2.1, where the higher concentration would be expected to have increased gel strength[27] and therefore an interface of enhanced resistance to liquid shear.

Values of μ_s for HPP solutions were in the range 10^{-3} g/s< μ_s <10^{-2} g/s for both concentrations, indicating a higher mobility of the hydrolysed protein chains at the interface than HPMC. This suggested that the HPP viscoelastic network at the interface was weaker than that of HPMC.

The values of μ_s for the Tween systems were in the extremely low range of 10^{-10} g/s< μ_s <10^{-8} g/s, where μ_s decreased with increasing liquid shear rate $\dot{\bar{\gamma}}_s$ in a manner similar to that observed by Clarke *et al.*[6] for a solution of SDS. At this stage, it is anticipated that the apparent surface shear thinning effect is related to the variation in surfactant population at the interface that was seen from the variation in PB surface tension (Fig. 7). A more complete analysis of the surface tension variability will be required in order to better understand this effect however.

It is important to remember that the values for D and subsequently μ_s were calculated for equilibrium PB systems ($R = R_e$), representing the maximum shear rates at any given liquid flow rates. In the Tween systems, values of R for a given PB profile could be over 3.5 times higher than the corresponding R_e value, decreasing shear rates by up to 2 orders of magnitude. By estimating values of D and μ_s based on the equilibrium PB trends in Fig. 9, this could yield values of D with magnitudes as high as 10^0 for the Tween systems, with subsequent values of μ_s in the order of 10^{-7}g/s. As the average D in a given region of PB profile is expected to scale with its inertial flow parameter, I (Fig. 8), this suggests the need to address the small variations in physical parameters that are likely to occur between the expansion and relaxation regions of the PB profile. Indeed, future work should seek to fit Eq. 12 separately to these regions, where it is expected that fit quality will further increase.

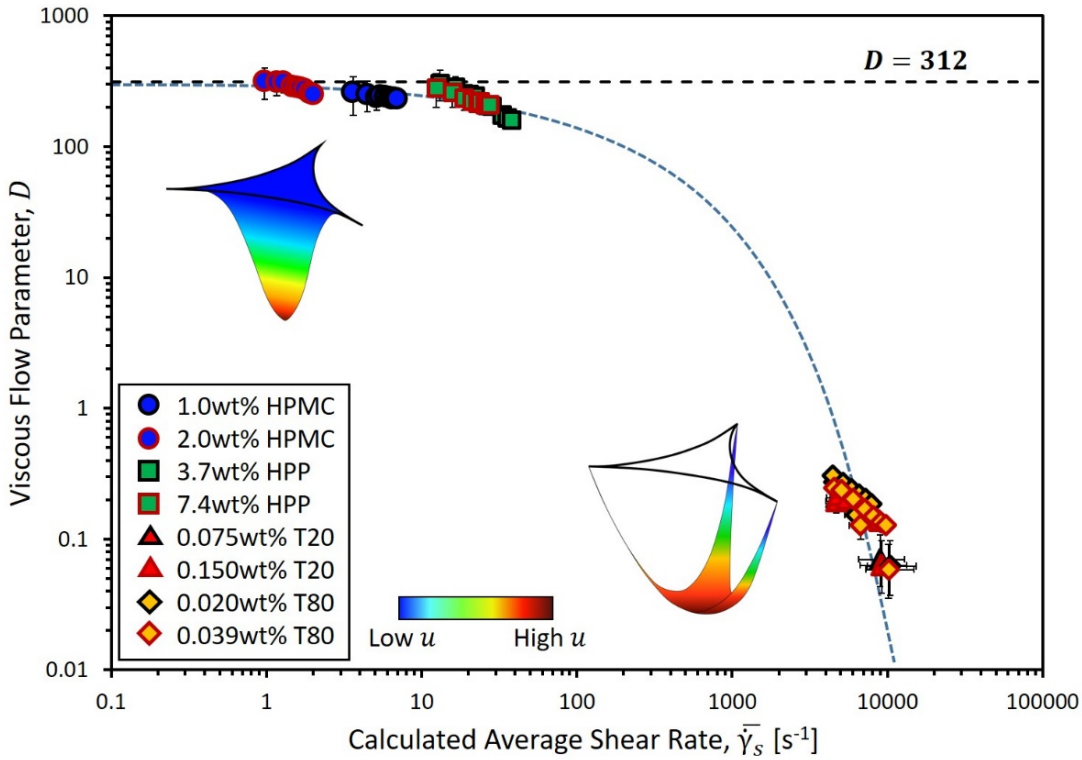

Figure 9. Viscous Flow Parameter, D, vs. Calculated Average Shear Rate, $\dot{\bar{\gamma}}_s$, for HPMC, HPP, Tween 20 and Tween 80 solutions. The physical limit of D = 312 is shown by black dashed line. Visualisations of liquid flow profiles are given alongside relevant data regions, where colours indicate liquid flow velocities, u, from low (blue) to high (dark red). Dashed blue line indicates the visible data trend and is included to guide the eye.

4. Conclusions

The novel experimental setup of Clarke*, et al.*[6] was further investigated using updated theory derived from the standard drainage theory[16] to model both PB relaxation and PB expansion in food grade surfactant systems. The updated theory was able to accurately describe the full length of measured PB profiles, including previously unexplained transitions between profile expansion and relaxation. The shapes and vertical heights of these transitions along the PB, Z_T, were shown to result from the difference between the equilibrium PB Radius, R_e, and the initial radius of the adjoining node, R_{n0}, where the change in PB radius with height was limited by the bulk and surface properties of the surfactant solutions. These transitions have so far been seen exclusively for the low molecular weight surfactant systems SDS[6], Tween 20 and Tween 80 where $R_e < R_{n0}$. However, the polymeric surfactant systems of HPP and HPMC also investigated here, demonstrated the inverted case of this distortion, where $R_e > R_{n0}$. To the knowledge of these authors, this is the first such case to be described in literature.

The fitting parameters R_e, surface tension, γ, and inertial flow parameter, I, were used to match theory to PB profiles at controlled liquid flow rates, Q. A single set of fitting parameters was used for each liquid flow rate, representing averaged values for the full PB profile. Despite this producing a good representation of these systems, it was shown that the increase in average PB radius of the PB expansion regions would have been expected to result in minor increases to the inertial flow parameter, I. As such, it is recommended that further investigation of LMWS solutions with this technique use separate fitting variables for PB relaxation and expansion regions.

While meaningful values for I and γ could not be obtained from fits to HPMC and HPP, the calculated values of the dissipative flow parameter, D, from R_e allowed a clear comparison between polymeric surfactants and LMWS to be made. Values for HPMC and HPP both tended towards the upper limit of D=312, with average values of D=263 for HPMC solutions and D=225 for HPP solutions. Values for Tween 20 and Tween 80 both tended towards the lower limit of D=0, with average values of D=0.17 for Tween 20 solutions and D=0.19 for Tween 80 solutions. These findings showed that the current technique was clearly able to differentiate between the viscous dominated and inertial dominated flow regimes.

Despite the expected clear separation of low and high mobility interfaces, it was noted that the accuracy with which the HPMC and HPP interfaces were characterised was relatively poor. This was primarily due to the need for highly accurate values of the bulk viscosity, μ, when calculating D, which was non-trivial for these non-Newtonian solutions. These errors were reduced at lower liquid flow rates however, where variations in μ produced less significant variations in calculated values of D.

Values of equilibrium PB μ_s for Tween 20 and Tween 80 solutions were within the range of 10^{-10} g/s$< \mu_s <10^{-8}$ g/s representing a virtually inviscid interface in both cases. A degree of surface shear thinning was observed in a similar manner to that of Clarke *et al.*[6] for SDS solution, which is proposed to be related to variations in surfactant population at the PB interface. This hypothesis was based on the observation of a single trend of increasing μ_s with increasing surface tension for regardless of surfactant concentration. A more in depth numerical analysis of these findings will be essential in establishing whether the occurrence of such

surface shear thinning for LMWS systems is a real effect or an artefact of the measurement technique.

Overall, the results presented here show that the PB-Node setup was able to describe highly complex PB profiles using bulk and interfacial physical variables that consistently fell within expected limits. Despite the lower accuracy in measuring the surface viscosities of polymeric surfactant systems, it was clear that the technique could clearly distinguish them from the extreme low surface viscosity LMWS systems of Tween 20 and Tween 80. Values calculated for LMWS surface viscosity clearly show them to be below the measurement sensitivity of conventional techniques as predicted in existing literature[22]. Therefore, it is believed by these authors that further analysis of such systems in this manner present a great opportunity to probe the fundamental mechanisms underlying LMWS surface viscosity in PB systems.

Supplementary Material

S1. Example of the relaxation-expansion transition region visually determined from a measured PB profile. (JPEG)

S2. Example of errors in the calculated viscous flow parameter, D, introduced by underestimating values of the bulk viscosity μ. The red curve represents the potential values of D for 2.0wt% HPMC at 180µl/min, where a range of values of μ are used in its calculation. The dashed blue line indicates the viscosity chosen for the calculation based on the average liquid shear rate, $\dot{\gamma}_s$. As this shear rate is expected to be an overestimation of that adjacent to the PB interface, the dotted blue line represents the maximum potential viscosity at this region based on measured flow curves of 2.0wt% HPMC. The resulting potential decrease in D is indicated by the red σ_D. The same calculations are applied for liquid flow rates of 100µl/min (orange) and 20µl/min (green), demonstrating the scaling of this error with liquid flow rate. (JPEG)

Acknowledgements

This work was supported by the EPSRC Centre for Innovative Manufacturing in Food. Fig. 4 was reproduced from Ref. [1] with permission from the Royal Society of Chemistry.

Corresponding Author

* Department of Chemical Engineering, University of Birmingham, Edgbaston, Birmingham, B15 2TT, UK

Author Contributions

The manuscript was written through contributions by all authors. All authors have given approval to the final version of the manuscript.

Funding Sources

This work was supported by the EPSRC Centre for Innovative Manufacturing in Food.

Abbreviations

CMC, critical micelle concentration; DOH, dodecanol; HPMC, hydroxypropyl methylcellulose; HPP, pea protein hydrolysate; LMWS, low molecular weight surfactant; PB,

Plateau border; SDS, sodium dodecyl sulphate; TTAB, tetradecyltrimethylammonium bromide; T20, Tween® 20; T80, Tween® 80.

References

1 J. Wang; A. V. Nguyen; S. Farrokhpay, A Critical Review of the Growth, Drainage and Collapse of Foams, *Advances in Colloid and Interface Science* **2016**, *228*, 55-70.

2 A. J. Green; K. A. Littlejohn; P. Hooley; P. W. Cox, Formation and Stability of Food Foams and Aerated Emulsions: Hydrophobins as Novel Functional Ingredients, *Current Opinion in Colloid & Interface Science* **2013**, *18*, 292-301.

3 R. J. Pugh, *Bubble and Foam Chemistry*; Cambridge University Press: Cambridge, United Kingdom, **2016**.

4 A. L. Ellis; A. B. Norton; T. B. Mills; I. T. Norton, Stabilisation of Foams by Agar Gel Particles, *Food Hydrocolloids* **2017**, *73*, 222-228.

5 ChunxiLi; MinglanLi; ZhixianShi; XueminYe, Effect of Soluble Surfactants on Vertical Liquid Film Drainage, *Physics of Fluids* **2019**, *31*, 032105.

6 C. Clarke; A. Lazidis; F. Spyropoulos; I. T. Norton, Measuring the Impact of Channel Length on Liquid Flow through an Ideal Plateau Border and Node System, *Soft Matter* **2019**, *15*, 1879-1889.

7 F. Elias; E. Janiaud; J.-C. Bacri; B. Andreotti, Elasticity of a Soap Film Junction, *Physics of Fluids* **2014**, *26*, 037101.

8 P. M. Kruglyakov; S. I. Karakashev; A. V. Nguyen; N. G. Vilkova, Foam Drainage, *Current Opinion in Colloid & Interface Science* **2008**, *13*, 163-170.

9 S. Naire; R. J. Braun; S. A. Snow, An Insoluble Surfactant Model for a Vertical Draining Free Film with Variable Surface Viscosity, *Physics of Fluids* **2001**, *13*, 2492-2502.

10 F. Rouyer; O. Pitois; E. Lorenceau; N. Louvet, Permeability of a Bubble Assembly: From the Very Dry to the Wet Limit, *Physics of Fluids* **2010**, *22*, 043302.

11 Q. SUN; L. TAN; G. WANG, Liquid Foam Drainage: An Overview, *International Journal of Modern Physics B* **2008**, *22*, 2333-2354.

12 S. S. Thete; C. Anthony; P. Doshi; M. T. Harris; O. A. Basaran, Self-Similarity and Scaling Transitions During Rupture of Thin Free Films of Newtonian Fluids, *Physics of Fluids* **2016**, *28*, 092101.

13 A. Anazadehsayed; N. Rezaee; J. Naser, Numerical Modelling of Flow through Foam's Node, *Journal of Colloid and Interface Science* **2017**, *504*, 485-491.

14 I. Cantat; S. Cohen-Addad; F. Elias; F. Graner; R. Höhler; O. Pitois; F. Rouyer; A. Saint-Jalmes; S. Cox, *Foams: Structure and Dynamics*; Oxford University Press: New York, **2013**.

15 A. Anazadehsayed; N. Rezaee; J. Naser; A. V. Nguyen, A Review of Aqueous Foam in Microscale, *Advances in Colloid and Interface Science* **2018**, *256*, 203-229.

16 D. Weaire; S. Hutzler; G. Verbist; E. Peters; I. Prigogine; S. A. Rice, A Review of Foam Drainage, *Advances in Chemical Physics* **1997**, *102*.

17 K. Koczó; G. Rácz, Flow in a Plateau Border, *Colloids and Surfaces* **1987**, *22*, 95-96.

18 M. Kostoglou; E. Georgiou; T. D. Karapantsios, A New Device for Assessing Film Stability in Foams: Experiment and Theory, *Colloids and Surfaces A: Physicochemical and Engineering Aspects* **2011**, *382*, 64-73.

19 O. Pitois; C. Fritz; M. Vignes-Adler, Liquid Drainage through Aqueous Foam: Study of the Flow on the Bubble Scale, *Journal of Colloid and Interface Science* **2005a**, *282*, 458-465.

20 O. Pitois; C. Fritz; M. Vignes-Adler, Hydrodynamic Resistance of a Single Foam Channel, *Colloids and Surfaces A: Physicochemical and Engineering Aspects* **2005b**, *261*, 109-114.

21 O. Pitois; N. Louvet; E. Lorenceau; F. Rouyer, Node Contribution to the Permeability of Liquid Foams, *Journal of Colloid and Interface Science* **2008**, *322*, 675-677.

22 Z. A. Zell; A. Nowbahar; V. Mansard; L. G. Leal; S. S. Deshmukh; J. M. Mecca; C. J. Tucker; T. M. Squires, Surface Shear Inviscidity of Soluble Surfactants, *Proceedings of the National Academy of Sciences* **2014**, *111*, 3677-3682.
23 D. Weaire; S. Hutzler, *The Physics of Foams*; Oxford University Press: New York, **1999**.
24 A. Saint-Jalmes; Y. Zhang; D. Langevin, Quantitative Description of Foam Drainage: Transitions with Surface Mobility, *Eur. Phys. J. E* **2004**, *15*, 53-60.
25 A. Saint-Jalmes, Physical Chemistry in Foam Drainage and Coarsening, *Soft Matter* **2006**, *2*, 836-849.
26 A. V. Nguyen, Liquid Drainage in Single Plateau Borders of Foam, *Journal of Colloid and Interface Science* **2002**, *249*, 194-199.
27 Dow, Methocel Cellulose Ethers Technical Handbook. The Dow Chemical Company: USA, 2002; p. 29. http://msdssearch.dow.com/PublishedLiteratureDOWCOM/dh_096d/0901b8038096d9ff.pdf?filepath=methocel/pdfs/noreg/192-01062.pdf&fromPage=GetDoc (accessed 24/07/2019).
28 M. C. Tulbek; R. S. H. Lam; Y. Wang; P. Asavajaru; A. Lam, Chapter 9 - Pea: A Sustainable Vegetable Protein Crop. In *Sustainable Protein Sources*, Nadathur, S. R.; Wanasundara, J. P. D.; Scanlin, L., Eds. Academic Press: San Diego, **2017**; pp 145-164.
29 K. L. Mittal, Determination of Cmc of Polysorbate 20 in Aqueous Solution by Surface Tension Method, *Journal of Pharmaceutical Sciences* **1972**, *61*, 1334-1335.
30 A. Patist; S. S. Bhagwat; K. W. Penfield; P. Aikens; D. O. Shah, On the Measurement of Critical Micelle Concentrations of Pure and Technical-Grade Nonionic Surfactants, *Journal of Surfactants and Detergents* **2000**, *3*, 53-58.
31 Anton-Paar Viscosity of Water. https://wiki.anton-paar.com/en/water/ **2008**. (accessed 18/04/2019).
32 K. Kinoshita; E. Parra; D. Needham, Adsorption of Ionic Surfactants at Microscopic Air-Water Interfaces Using the Micropipette Interfacial Area-Expansion Method: Measurement of the Diffusion Coefficient and Renormalization of the Mean Ionic Activity for Sds, *Journal of Colloid and Interface Science* **2017**, *504*, 765-779.
33 J. C. Earnshaw, Surface Viscosity of Water, *Nature* **1981**, *292*, 138-139.

Table of Contents